Model Reduction for Synchronizing Stability of BPS-Connected IBRs: Constant Impedance-based Network Assumption

Lingling Fan, *Fellow, IEEE*, Zhixin Miao, *Senior Member, IEEE*,
Rahul H. Ramakrishna, *Graduate Student Member, IEEE*, Deepak Ramasubramanian, *Senior Member, IEEE*

***Abstract*—The popular power system dynamic simulation and analysis tools, e.g., PSS/E, PSLF, TSAT, and PowerWorld, adopt the assumption of constant or algebraic impedance representation for passive transmission networks. This paper investigates whether such a modeling framework is adequate for synchronizing stability simulation and analysis of bulk power system (BPS)-connected inverter-based resources (IBRs). We demonstrate that this framework is suitable for grid-following synchronizing-related dynamics below 10 Hz. We point out the exact reason that makes constant impedance assumption valid. If the underlying mechanism of dynamics is associated with the imaginary part of the complex grid impedance, then the constant impedance assumption is valid. However, if the underlying mechanism is associated with the real part of the complex grid impedance, then such assumption is no longer valid and we have to either resort to electromagnetic transient (EMT) simulation or adjust the network modeling assumption.**

***Index Terms*—Complex grid impedance, inverter-based resource, stability, model reduction, algebraic impedance.**

I. Introduction

SYSTEM level dynamic studies for bulk power system (BPS)-connected inverter-based resources (IBRs) mainly concern with synchronizing-related stability issues, including both transient stability and small-signal stability issues. Both are related to synchronizing units of IBRs. In the context of conventional synchronous generators, both transient stability and electromechanical oscillations issues are related to a generator's swing dynamics or a feedback system relating real power and synchronizing angle. In the case of grid-following IBRs, their phase-locked loops (PLLs) are the synchronizing units which generate a synchronizing angle with an input from the terminal voltage.

Traditional root mean square (RMS)-based tools for system-level dynamic studies, e.g., PSS/E, PSLF, TSAT and PowerWorld, rely on a modeling framework which treats a passive transmission network as an constant or algebraic admittance matrix. Constant impedance is based on the nominal frequency. PSS/E's dynamic simulation has an option "Network Frequency Dependence", which models network reactances or susceptances as varying with the instantaneous local frequency. This type of impedance is denoted as "transient algebraic impedance" after [1]. The term "transient algebraic impedance" was coined after the 1993 paper by Peter Sauer and coauthors titled "Transient algebraic circuits for power system dynamic modeling" [2]. This simplification ensures a reduced order for the overall dynamic system by treating the network's voltage and current relationship as algebraic and in turn, a fast simulation speed, thereby providing the capability of handling large-scale system.

It is well known that IBRs are based on power electronic converters and the converter control has a wide range of dynamics. This fact in turn leads to wideband dynamics observed in real world for IBRs. While EMT simulation is for sure the only choice for those dynamics related to inductance and capacitance of transmission lines (e.g., subsynchronous resonances related to electrical LC modes), we would like to examine for synchronizing unit related system-level dynamics, whether the constant admittance network assumption can still be adopted and help stability analysis.

In real-world operation, 3 Hz to 4-Hz oscillation events have been reported in Texas wind farms [3] and Hydro One solar PV and wind farms [4]. System-wide 8-Hz voltage oscillation events have occurred twice in Scotland in 2021 and 2023 [5]. While these events have all been classified as weak grid oscillation events in the IEEE PES IBR SSO task force paper [6], it is now understood that those voltage oscillations are also associated with real power and PLLs. Therefore, those oscillation events are indeed related to synchronizing stability.

The research goal of this paper is to determine whether those events can be modeled by traditional stability analysis tools (e.g., PSS/E). Prior research has been conducted by industry experts to compare these tools against EMT simulation tools for IBR dynamics, e.g., [7]. The finding from [7] is that adequate IBR models in PSS/E can help improve the accuracy for many low-frequency dynamics. On the other hand, the reason behind has not been spelled out and an in-depth analysis is mostly desired.

Contributions: To this end, we propose to first examine a single-source infinite-bus testbed. We examine the synchronizing dynamics in the perspective of the grid impedance in the dq-frame or the complex grid impedance, and identify which part of the complex grid impedance plays a major role in synchronization dynamics. It is found that if the imaginary part plays the major role, the constant impedance assumption can capture the dynamics. On the other hand, if the real part plays the major role, the constant impedance assumption will

This project is supported in part by EPRI and in part by DOE DE-EE0011474. L. Fan, Z. Miao, and Rahul H. Ramakrishna are with the Department of Electrical Engineering, University of South Florida, Tampa, FL, 33620 (e-mail: linglingfan@usf.edu). D. Ramasubramanian is with EPRI.

not be able to capture the dynamics.

This research provides a fundamental understanding on model reduction and has significant practical values in this energy transition era. We offer a perspective from frequency domain, which differs significantly from the traditional systematic model reduction method based on singular perturbation. Singular-perturbation method starts from a time-domain state-space model and separates state variables based on time scale. This method has been used to derive reduced-order power system dynamic models in the 1990s, *e.g.*, [8], and recently been used to derive aggregated models for IBR networks [9]. While the singular perturbation method leads to reduced-order models suitable for slow dynamics, it cannot provide a quantitative modeling guideline to describe how slow is slow. Similarly, it cannot answer this type of questions: Are 8-Hz oscillations associated with IBRs slow or fast, and can they be replicated using RMS-based simulation.

Our research provides answers and shows why the RMS-based tools can work for IBRs in what types of conditions. This research also delves into the technical depth to show how dynamics are related to the complex grid impedance and how the entanglement with either the real part or the imaginary part can be used for model reduction.

Structure: The rest of the paper is organized as follows. Section II presents complex grid impedance, a frequency-domain notion. Section III presents the synchronizing feedback system for the IBR grid integrated system. Section IV presents the simulation results and comparison of different modeling assumptions. Section V summarizes this paper.

II. Complex Grid Impedance

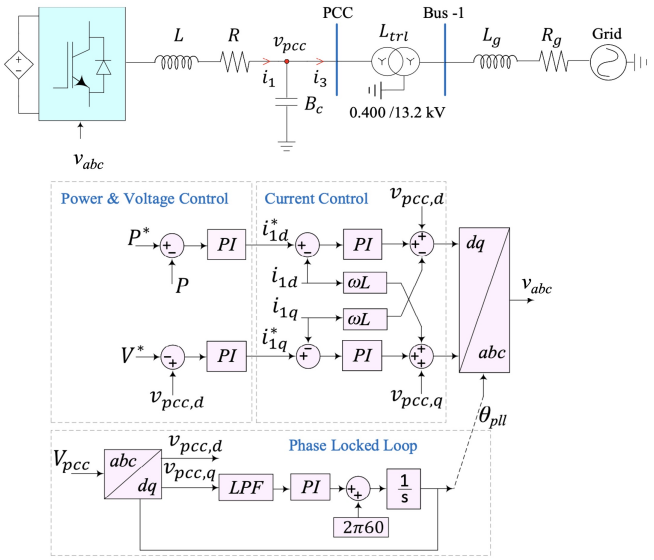

Fig. 1: The testbed of a single IBR connected to an infinite bus. The IBR control block diagram is also presented.

When conducting synchronization related analysis, it is common to adopt the synchronous rotating frame (the rotating speed is ω_0) or the dq frame, instead of the static frame where three-phase currents and voltages are sinusoidal. In the synchronous rotating frame, the currents and voltages are constant at steady state. This makes power and angle related computation and analysis very easy.

In the dq frame, an impedance becomes a complex impedance. Take the example of an RL impedance, its impedance can be expressed as $R+Ls$ in the static frame. In the dq frame , this impedance is expressed as $R+L(s+j\omega_0)$. It can be seen that this impedance is a frequency-domain complex impedance, with the $R+Ls$ as its real part and $\omega_0 L$ as its imaginary part. It is very easy to see that the imaginary part of the grid impedance keeps constant, while the real part $R+Ls$'s magnitude increases when the evaluating frequency increases.

The complex impedance has a form of $Z_{\text{real}}+jZ_{\text{imag}}$. In the following, we show that the real and imaginary components of the impedance further form a 2-by-2 matrix mapping the active current and the synchronizing angle to the point of interconnection (POI) dq voltages.

Fig. 1 shows a typical single IBR grid integration circuit and the IBR's grid-following control block diagram. The parameters of the testbed and the control block are given in Tables III and IV in Section IV. For system-level dynamic performance analysis, high-frequency dynamics above 100 Hz are usually ignored. In this context, an IBR can be assumed as a current source synchronized to the grid through a synchronizing unit, e.g., a PLL or a power-frequency droop control. The output from the synchronizing unit is notated as δ. The circuit diagram is shown in Fig. 2.

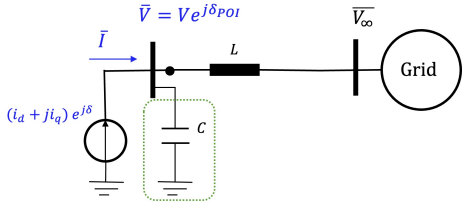

Fig. 2: An IBR is integrated to a grid. The grid may have different characteristics: without compensation or shunt compensation.

This IBR can be viewed as a controlled current source (i_d+ji_q) in the PLL frame. In the ~~system~~grid dq frame, the PLL's angle against the system's d-axis is notated as δ. Therefore, in the ~~system~~grid dq frame, the current source is notated as

$$\bar{I} = (i_d + ji_q)e^{j\delta}.$$

The grid may be represented as a Thévenin equivalent: a constant voltage source $\bar{V}_\infty$ behind an impedance, representing the transmission line. If the transmission line is not series compensated, we may use a pure inductor L to represent it. We may use X_L to represent the reactance of the inductor at the nominal frequency ω_0, where $\omega_0 = 377$ rad/s.

A. No shunt compensation

If there is no shunt compensation, the complex impedance of the grid (viewed from the POI bus) Z can be expressed as follows:

$$Z = sL + jX_L,\ \ Z_{\text{real}} = sL,\ Z_{\text{imag}} = \omega_0 L = X_L. \qquad (1)$$

A complex impedance or admittance, is essentially a complex transfer function, describing the relationship between complex vectors. In 2007, L. Harnefors presented many use cases of complex transfer functions in [10].

It can be seen that Z_{imag} is a constant while Z_{real}'s magnitude increases if the frequency increases.

Based on the circuit topology, the voltage phasor can be expressed in terms of the IBR current and the line impedance Z.

$$\overline{V} = Z\overline{I} + \overline{V}_{\infty}. \tag{2}$$

where $\overline{I} = (i_d + ji_q)e^{j\delta}$ and $\overline{V} = Ve^{j\delta_{\text{POI}}}$.

Assume that the grid source voltage is kept constant, the small-signal relationship between the POI voltage phasor and the IBR current phasor can be expressed as follows:

$$\Delta\overline{V} = Z\Delta\overline{I}. \tag{3}$$

In the grid dq frame, the current and voltage complex phasors are expressed as follows:

$$\overline{I} = (i_d + ji_q)e^{j\delta},\ \overline{V} = Ve^{j\delta_{\text{POI}}}. \tag{4}$$

The corresponding small-signal expressions are:

$$\Delta\overline{I} = \left((\Delta i_d + j\Delta i_q) + j(i_d + ji_q)\Delta\delta\right)e^{j\delta_0}, \tag{5}$$
$$\Delta\overline{V} = (\Delta V + Vj\Delta\delta_{\text{POI}})e^{j\delta_{\text{POI},0}}. \tag{6}$$

where the subscript 0 notates the initial steady-state condition.

To arrive at a much concise expression, another system dq frame—the POI dq frame—is introduced. Fig. 3 shows the three frames: the grid dq frame, the POI dq frame, and the PLL dq frame. The first two frames have a constant rotating speed of the nominal value ω_0. They are separated by an angle. This angle is the POI bus voltage's initial phase angle relative to the grid voltage $\delta_{\text{POI},0}$. The PLL's frame aligns with the POI frame at the initial steady state, since the PLL's output angle tracks the POI bus' voltage angle. The angle between the PLL frame and the grid frame is δ, which varies during dynamics. Similarly, the POI voltage's phase angle δ_{POI} varies during dynamics.

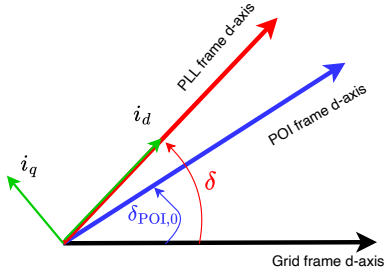

Fig. 3: Geometric relationship of the three dq frames.

In the POI dq frame, their expressions becomes:

$$\overline{I} = (i_d + ji_q)e^{j(\delta - \delta_{\text{POI},0})},\ \overline{V} = Ve^{j(\delta_{\text{POI}} - \delta_{\text{POI},0})} \tag{7}$$

At the initial steady-state condition, these two conditions hold: $\delta - \delta_{\text{POI},0} = 0$ and $\delta_{\text{POI}} - \delta_{\text{POI},0} = 0$. Therefore, in the POI dq frame, their small-signal expressions become:

$$\Delta\overline{I} = (i_d + ji_q)j\Delta\delta + \Delta i_d + j\Delta i_q$$
$$\Delta\overline{V} = \Delta V + jV\Delta\delta_{\text{POI}}. \tag{8}$$

Assume that $i_q \approx 0$ ~~or~~, that is the reactive power exported from the IBR $Q \approx 0$, and $\Delta i_q \approx 0$ (there is no control to adjust i_q). We get:~~Also assume that at the initial steady-state condition δ_{POI} and δ are 0° (the dq frame aligns with the initial POI voltage space vector). Then:~~

$$\Delta\overline{I} = \Delta i_d + ji_d\Delta\delta,\ \ \Delta\overline{V} = \Delta V + jV\Delta\delta_{\text{POI}}. \tag{9}$$

Therefore, (3) becomes:

$$\Delta V + jV\Delta\delta_{\text{POI}} = (Z_{\text{real}} + jZ_{\text{imag}})(\Delta i_d + ji_d\Delta\delta). \tag{10}$$

It can be seen that

$$\begin{bmatrix}\Delta V \\ V\Delta\delta_{\text{POI}}\end{bmatrix} = \begin{bmatrix}Z_{\text{real}} & -Z_{\text{imag}} \\ Z_{\text{imag}} & Z_{\text{real}}\end{bmatrix}\begin{bmatrix}\Delta i_d \\ i_d\Delta\delta\end{bmatrix}. \tag{11}$$

Based on (11), it can be seen that the POI voltage is influenced by both the initial d-axis current and the synchronizing angle. In the low-frequency region, or for the low-frequency dynamics (e.g., less than 10 Hz), $|Z_{\text{real}}| \ll |Z_{\text{imag}}|$. Therefore, for the slow dynamics, voltage is influenced mainly by the synchronization angle while the POI angle is influenced mainly by the active current i_d.

B. Shunt compensation

If there is shunt compensation at the POI bus, the voltage and current phasors' relationship in the ~~system~~grid dq frame is shown as follows:

$$(s + j\omega_0)L \cdot \left[\Delta\overline{I} - (s + j\omega)C\Delta\overline{V}\right] = \Delta\overline{V}. \tag{12}$$

Rearrange the above equation and we can find the equivalent impedance Z viewed from the inverter's perspective.

$$\underbrace{\frac{(s + j\omega_0)L}{1 + LC(s + j\omega_0)^2}}_{Z} \cdot \Delta\overline{I} = \Delta\overline{V} \tag{13}$$

Z_{real} can be found through taking the real part of Z:

$$Z_{\text{real}} = sL\frac{1 + LC(s^2 + \omega_0^2)}{1 + 2LC(s^2 - \omega_0^2) + (LC)^2(s^2 + \omega_0^2)^2}. \tag{14}$$

The series inductance's reactance at the nominal frequency is notated as X_L and $X_L = \omega_0 L$. The shunt capacitor's susceptance at the nominal frequency is notated as B_c and $B_c = \omega_0 C$. Eq. 14 can be written as:

$$Z_{\text{real}} = \frac{s}{\omega_0}X_L\frac{1 + X_L B_C\sigma_\omega}{(1 + X_L B_C\sigma_\omega)^2 - 4X_L B_C}. \tag{15}$$

where $\sigma_\omega = 1 + (s/\omega_0)^2$.

Similarly, Z_{imag} can be found as follows.

$$Z_{\text{imag}} = X_L\frac{1 - X_L B_C\sigma_\omega}{(1 + X_L B_C\sigma_\omega)^2 - 4X_L B_C} \tag{16}$$

It can be seen that when $s = j0$, or at the steady-state condition,

$$Z_{\text{real}}(j0) = 0, \;\; Z_{\text{imag}}(j0) = \frac{X_L}{1 - X_L B_C}. \tag{17}$$

C. Shunt and Series Compensation

If there are both shunt compensation at the POI and series compensation in the transmission line, the equivalent grid impedance viewed from the IBR in the static frame becomes:

$$Z^{\text{static}} = \frac{Z_{\text{shunt}} Z_{\text{series}}}{Z_{\text{shunt}} + Z_{\text{series}}} = \frac{\frac{1}{sC}(sL + \frac{1}{sC_1})}{\frac{1}{sC} + sL + \frac{1}{sC_1}}, \tag{18}$$

where C_1 is the series capacitor's capacitance.

The above equation can be expressed using the nominal reactance X_L for the inductor, X_C for the series capacitor, and susceptance B_c for the shunt capacitor. Additionally, X_C may be replaced by KX_L where K is the compensation level.

$$Z^{\text{static}} = s_1 X_L \frac{1 + \frac{K}{s_1^2}}{1 + s_1^2 X_L B_C \left(1 + \frac{K}{s_1^2}\right)}, \tag{19}$$

where $s_1 = s/\omega_0$ and ω_0 is the nominal frequency.

In the dq frame, s should be replaced by $s + j\omega_0$. In turn, s_1 should be replaced by $s_1 + j$. The grid impedance becomes a complex s-domain impedance:

$$Z = (s_1 + j) X_L \frac{1 + \frac{K}{(s_1+j)^2}}{1 + (s_1 + j)^2 X_L B_C \left(1 + \frac{K}{(s_1+j)^2}\right)} \tag{20}$$

It is quite challenging to find the closed-form expression for $Z_{\text{real}}(s)$ and $Z_{\text{imag}}(s)$. On the other hand, the frequency responses of $Z_{\text{real}}(j\omega)$ and $Z_{\text{imag}}(j\omega)$ can be found numerically by first evaluating $Z(j\omega)$ fort $s = j\omega$ or $s_1 = j\frac{\omega}{\omega_0}$, and then evaluating $Z^*(j\omega)$ for $s = j\omega$ or $s_1 = j\frac{\omega}{\omega_0}$.

The expression of Z^* can be easily found based in (20):

$$Z^* = (s_1 - j) X_L \frac{1 + \frac{K}{(s_1-j)^2}}{1 + (s_1 - j)^2 X_L B_C \left(1 + \frac{K}{(s_1-j)^2}\right)} \tag{21}$$

The numerical complex values of $Z_{\text{real}}(j\omega)$ and $Z_{\text{imag}}(j\omega)$ can be found as:

$$Z_{\text{real}}(j\omega) = \frac{Z(j\omega) + Z^*(j\omega)}{2} \tag{22}$$

$$Z_{\text{imag}}(j\omega) = \frac{Z(j\omega) - Z^*(j\omega)}{j2} \tag{23}$$

D. Constant Impedance

Starting from the s-domain impedance expression viewed in the static frame (19), constant impedance refers to the one evaluated at $s = j\omega_0$ or $s_1 = j1$. Therefore,

$$Z_{\text{constant}} = jX_L \frac{1 - K}{1 - X_L B_C (1 - K)} = jZ_{\text{imag}}(j0), \tag{24}$$

A numerical case is examined: an inductive grid with both shunt and series compensation. The real and imaginary parts of the complex grid impedance of a system with $X_L = 0.4$, $X_C = 0.2$, and $B_C = 0.0803$) are shown in Fig. 4a. It can be seen from Fig. 4a that in the frequency region below 5 Hz, the magnitude of Z_{imag} is 4 times more than Z_{real}. At 10 Hz, Z_{imag} is about 2 times of Z_{real}. At 17 Hz, the two have the same magnitudes. For the 25% compensation level, the two have the same magnitudes at 30 Hz.

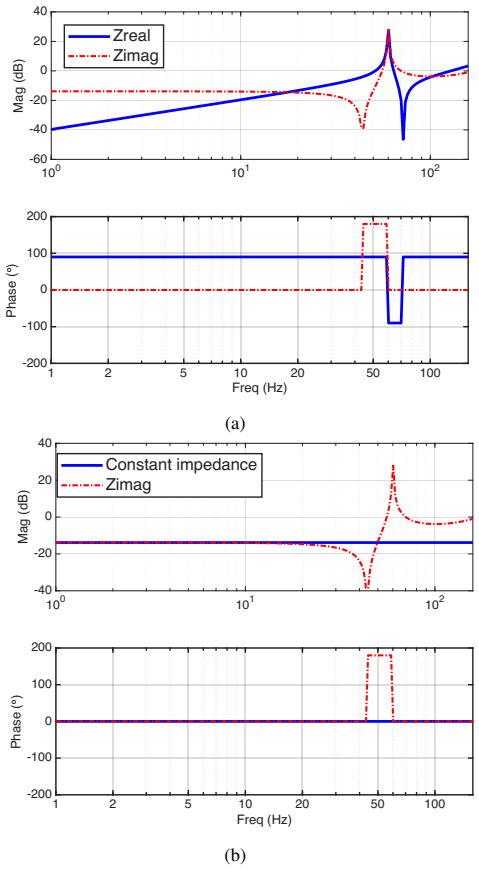

Fig. 4: Grid impedance including both shunt and series compensation. (a) Frequency responses of Z_{real} and Z_{imag}. (b) Comparison of Z_{imag} and the constant impedance. $X_L = 0.4$, series compensation $X_C = 0.2$, and shunt compensation $B_C = 0.0803$.

Fig. 4b shows the comparison of Z_{imag} and the constant impedance evaluated at the nominal frequency. It can be seen that for the frequency region below 20 Hz, these two match very well.

Remarks: Complex grid impedance analysis leads to the two remarks. (i) In the below 20 Hz region, Z_{imag} is relatively constant, and can be represented by a constant impedance. (ii) The magnitude of Z_{real} is less than Z_{imag} in the low-frequency region.

III. Feedback System of Synchronization

Based on (11), in addition to the real power expression ($\Delta P = V\Delta i_d + i_d \Delta V$), and power control, a feedback system is formed and shown in Fig. 5. Assume that the IBR's d-axis outer control is in real power regulation mode and the PI controller G_P can be expressed as $G_P = K_p + K_i/s$ ($K_p = 0.25$, $K_i = 25$). The negative feedback power controller generates the d-axis current order i_d^*, which further influences i_d. The inner current controller's effect is modeled as a first-order lag $\frac{1}{1+\tau s}$ where τ is chosen based on the

current control bandwidth (e.g., 0.001 s for a bandwidth of 1000 rad/s).

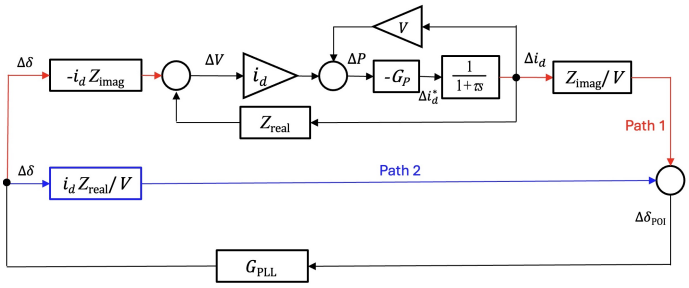

Fig. 5: The feedback system showing the synchronizing loop. The adders are all based on "+" signs and these signs are omitted to avoid making the diagram too crowded.

The feedback system consists of three main components: Path 1, Path 2 and the PLL. The PLL tracks the POI bus' phase angle δ_{POI} and its transfer function has the input as the POI angle and the output as the synchronizing angle δ. For a PLL with a second-order low-pass filter, its closed-loop transfer function is shown as follows when the voltage magnitude is assuming as 1 pu.

$$G_{\text{PLL}} = \frac{\Delta\delta}{\Delta\delta_{\text{PCC}}} = \frac{G_{\text{LPF}}\left(K_p + \frac{K_i}{s}\right)\frac{1}{s}}{1 + G_{\text{LPF}}\left(K_p + \frac{K_i}{s}\right)\frac{1}{s}}, \tag{25}$$

where $G_{\text{LPF}} = \frac{\omega_f^2}{s^2+2\zeta\omega_f s+\omega_f^2}$, $\zeta = 0.707$ and ω_f is the resonant frequency (e.g., $2\pi \times 25$ rad/s).

It can be seen that the synchronizing angle δ influences the POI angle δ_{POI} through two paths: Path 1 and Path 2. In Path 1, δ influences voltage, and further influences the real power. Through the real power control, i_d is influenced. Furthermore, i_d influences the POI angle. In Path 1, Z_{imag} plays a major role. In Path 2, δ directly influences the POI angle through the Z_{real}.

Remarks: The feedback system on synchronization shows that there are two paths for a synchronizing angle influences the voltage phase angle. In Path 1, Z_{imag}'s effect is dominant, while in Path 2, Z_{real}'s effect is dominant. It can be expected that for dynamics below 10 Hz region, Path 1 is the dominant path while for dynamics above 10 Hz region, Path 2's effect cannot be ignored. In the 20-Hz and above region, Path 2 becomes the dominant path.

A. Simplified versions based on constant grid impedance

In fact, the simplified version of the feedback system presented in Fig. 5 has been shown in prior research. When we consider the grid impedance as a pure reactance and further ignore the dynamics of the inductor, $Z_{\text{real}} = 0$ and $Z_{\text{imag}} = X$. The feedback system becomes similar to the diagram derived in [11]–[13].

Using the constant impedance assumption, the effect of Path 2 is ignored. Fig. 6 shows the two simplified feedback systems. Fig. 6(a) ignores the effect of Δi_q or the q-axis outer control has no impact on ΔV, while Fig. 6(b) includes the effect of AC voltage control by including Block2. Block2's expression has been derived in our prior research [11] and the derivation procedure is shown as follows.

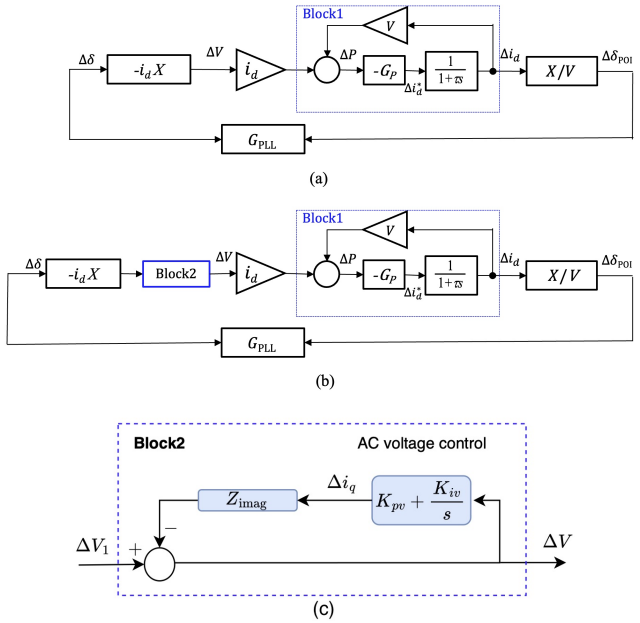

Fig. 6: The simplified versions of the feedback system. (a) $\Delta i_q \approx 0$, (b) $\Delta i_q \neq 0$ and the voltage control is included. (c) Block 2.

Assume at the initial condition $i_q = 0$ or $Q = 0$. However, $\Delta i_q \neq 0$ due to AC voltage control. then $\Delta\overline{I} = \Delta i_d + j(\Delta i_q + i_d\Delta\delta)$. The POI voltage has the following relationship with Δi_d, Δi_q and $\Delta\delta$.

$$\Delta V = \underbrace{Z_{\text{real}}\Delta i_d - Z_{\text{imag}} i_d \Delta\delta}_{\Delta V_1} - Z_{\text{imag}}\Delta i_q. \tag{26}$$

A block diagram is shown in Fig. 6(c).

$$\text{Block2} = \frac{1}{1 + \left(K_{pv} + \frac{K_{iv}}{s}\right) Z_{\text{imag}}} = \frac{s}{(1+K_{pv})s + K_{iv}X}. \tag{27}$$

It can be seen that Block2 is a high-pass filter.

B. Comparison of two assumptions

In the following, we compare the stability analysis results based on the constant impedance modeling assumption and the detailed grid impedance model. Table I lists the two modeling assumptions.

TABLE I: Comparison of Impedance Modeling Assumptions

comments	constant Z	detailed Z
Z_{real}	0	$\frac{s}{\omega} X_L \frac{1+X_L B_C \sigma_\omega}{(1+X_L B_C \sigma_\omega)^2 - 4X_L B_C}$
Z_{imag}	$\frac{X_L}{1-X_L B_C}$	$X_L \frac{1-X_L B_C \sigma_\omega}{(1+X_L B_C \sigma_\omega)^2 - 4X_L B_C}$

For $X_L = 0.6720$, $B_c = 0.0803$, Path 1 (the black line), Path 2 (the green line) and Path (Path 1+Path 2, the red line) are examined and their Bode diagrams are compared for the two modeling assumptions. Fig. 7 shows the comparison. For the detailed Z, it can be seen that the overall path's frequency response is influenced mainly by Path 1 in the below 10 Hz region and by Path 2 in the above 20 Hz region. The dominant influencer of Path 1 is Z_{imag}, while the dominant influencer of Path 2 is Z_{real}. Therefore, it can also be stated that the

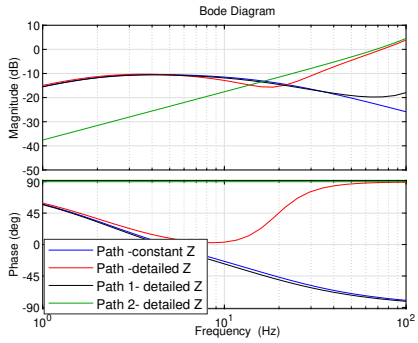

Fig. 7: Comparison of Path for two types of impedance models.

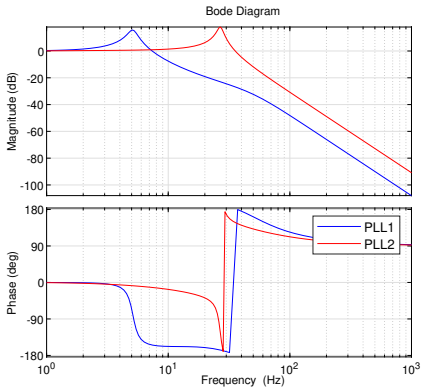

Fig. 8: Closed-loop transfer functions' Bode diagram for two PLLs.

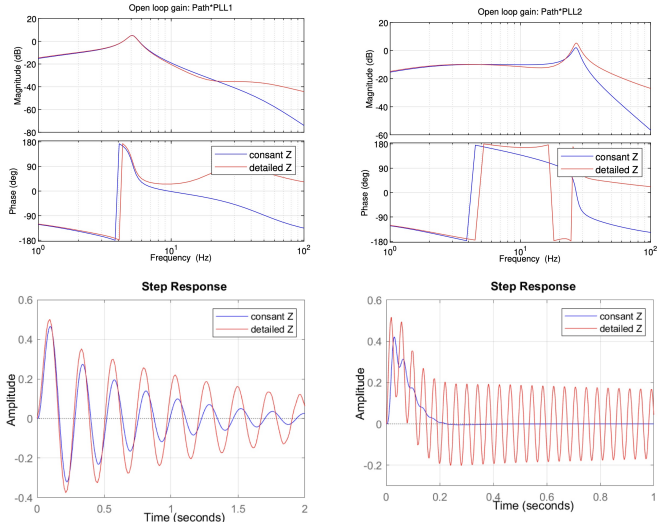

Fig. 9: Stability analysis results. Upper row: Bode diagrams of the open loop gains for two cases (PLL1, and PLL2). Lower row: step responses for the two closed-loop systems. Left: 5-Hz oscillation case. Right column: 20-Hz oscillation case.

overall frequency response (from the synchronization angle to the POI angle) is influenced mainly by Z_{imag} in the below 10 Hz region and by Z_{real} in the above 20 Hz region.

For the constant Z assumption, the transfer function Path (shown in blue) has very similar response compared to Path 1 of the detailed Z assumption (the black line).

- The frequency responses for the below 10 Hz region (blue and red) for the two impedance assumptions are similar.
- However, for the 10 Hz -20 Hz region, their phasor angles deviate from each other.
- In the above 20-Hz region, both magnitudes and angles are quite different.

Remarks: The frequency responses show that for the below 10 Hz dynamics, constant Z assumption appears adequate. On the other hand, for above 10 Hz dynamics, constant Z assumption is not adequate.

C. *Frequency-domain analysis results*

Two case studies are presented to demonstrate the influence of Z assumption. Fig. 8 shows the two types of PLLs. PLL1 has a peak at 5 Hz while PLL2 has a peak at 26 Hz. The PLL parameters are tuned to create resonances in a subsystem, which may influence the overall feedback and create oscillations. It is to be clarified that resonances in a subsystem is just one of the mechanisms of oscillations. There are many other types of causes of oscillations, e.g., communication delay [6], [14]. The purpose is to create oscillations of different frequency for further modeling investigation, rather to create an exhaustive list of oscillations due to different mechanisms.

The open loop gains are shown in Fig. 9, along with the step responses of the closed-loop systems. It can be clearly seen that the interaction of PLL1 and the rest of the system introduces 4-Hz oscillations. The constant Z model can capture the oscillations. The interactions of PLL2 and the rest of the system introduces 20 Hz oscillations. The constant Z model cannot capture the 20-Hz oscillations.

IV. Nonlinear Simulation Results

In this section, we present the comparison of the detailed analytical model (Model 1) versus the reduced-order model (Model 2, constant Z). Building analytical models for IBR grid integration systems have been covered by the senior authors' book [15] and a recent magazine paper [16]. Compared to commercial EMT simulation packages, e.g., PSCAD or MATLAB/Simscape, the analytical models are based on *dq* frames, instead of the static *abc* frame. In turn, the state variables are constant at steady state. This feature enables Jacobian linearization for a given initial operating condition, which further leads to small-signal analysis.

Additionally, we introduce Model 3, another reduced-order model, where X_L and B_c are not constant, rather variant according to the PLL's frequency. Model 3 has been proposed in [1]. It considers part of the EMT dynamics of the transmission network. The two reduced-order models are of the same order. In Model 2, the GFL is assumed as a current source synchronized to the grid through a PLL while the transmission line is represented as a constant impedance. The inner current control loop of a GFL is typically designed with a high control bandwidth (e.g., greater than 150 Hz). Therefore, the current tracking dynamics are much faster than the slower system dynamics, such as real power and voltage regulation, as well as the angle tracking dynamics determined by the PLL. For this reason, an IBR can be reasonably approximated as a current source. Accordingly, in this paper, a first-order unit is used to represent the IBR as a current source in the PLL reference frame.

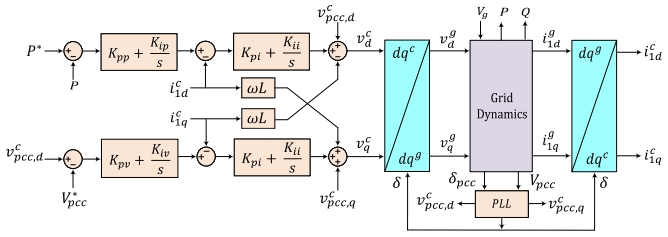

(a)

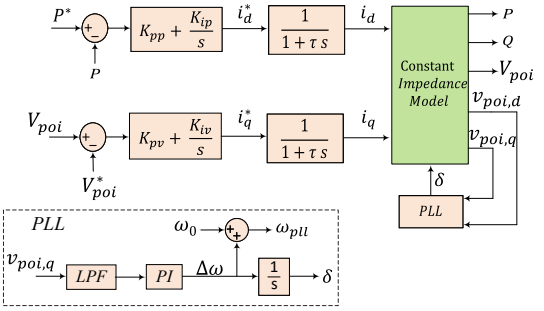

(b)

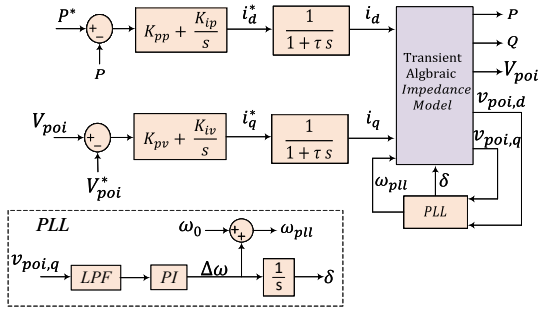

(c)

Fig. 10: Interconnection diagrams. (a) Model 1. (b) Model 2- constant Impedance Model. (c) Model 3 - transient algebraic model.

Model 3 uses the same assumption as Model 2, except that the transmission line is represented as a transient impedance where its reactance varies according to the PLL frequency. Table II presents the modeling assumptions for the three models. The diagrams of the three models are shown in Fig. 10. It can be seen that if the grid dynamic block in Model 1 is replaced by an algebraic relationship, this model (Model 1a) retains the IBR control structure, while treats the network impedance as constant. Model 1a has been tested and it is found its performance is similar to Model 2. Therefore, results based on Model 1a are not presented in the paper.

TABLE II: Comparison of Modeling Assumptions.

	comments	# of state variables for the LCL circuit	IBR modeling assumption
Model 1	EMT	6	voltage source, with current feedback control
Model 2	constant impedance	0	current source, ignoring current feedback control
Model 3	transient impedance	0	current source, ignoring current feedback control

All three models are built in the dq-frame. For the balanced operating conditions, each model has an equilibrium point and can be linearized around the equilibrium point. Eigenvalues can be calibrated based on those linearized models. Interested readers may refer to [16] on the procedure of obtaining linearized models and conducting eigenvalue analysis.

TABLE III: Parameters of the electric system.

Description	Item	Values
Rated Power	S_{base}	100 MW
Inverter terminal voltage	V_p	400 V
Medium voltage	V_{POI}	13.2 kV
Nominal frequency	ω_0	377 rad/s
Filter (RL)	Z_{RL}	$0.003 + j0.108$ pu
Filter (C)	B_C	0.0803 pu
Transformer impedance	Z_T	$0.02 + j0.0721$ pu
Grid line impedance	R_g	$0.1X_g$
	X_g	0.4 pu

TABLE IV: Parameters of the plant and inverter-level controls.

Description	Item	Values	Bandwidth
Current control	PI	$0.3 + 6/s$ p.u.	170 Hz
Real power control	PI	$0.25 + 25/s$ p.u.	3.3 Hz
AC Voltage control	PI	$0.4 + 40/s$ p.u.	5 Hz
Inverter-level PLL	PI	$10 + 1000/s$ p.u.	8 Hz

A. 4-Hz oscillation event

Model 1 and Model 2 have been built for comparison. With the same operating conditions, they are compared for the eigenvalue loci. The GFL's control parameters have been tuned to create a 4-Hz oscillation event.

Fig. 11(a) shows the comparison of Model 1 and Model 2 on time-domain simulation results for the 4-Hz oscillation event. It can be seen that Model 1 and Model 2 can provide very similar simulation results for the four line tripping events. Both show 4-Hz oscillations become severe if the grid impedance increases.

Fig. 11(b) shows the comparison of Model 1 and Model 2 on the eigenvalue loci. It can be seen that the dominant 4-Hz modes can be captured by Model 2.

B. 20-Hz oscillation event

In the second case, the PLL parameters of the IBR are adjusted to create 20-Hz oscillations for a line tripping event. The second-order LPF's resonance frequency is assumed to 25 Hz while the PI controller is $120+2000/s$. The PLL's closed-loop transfer function notates the output angle versus the input angle's relationship. Its frequency-domain response is shown in Fig. 8, labeled as "PLL2". It can be seen that compared to PLL1, PLL2 has a peak at about 20 Hz.

Fig. 12(a) shows the comparison of Model 1, Model 2, and Model 3 on time-domain simulation results for the 20-Hz oscillation event. Fig. 12(b) shows the comparison of the three models on the eigenvalue loci. It can be seen that the 20-Hz mode cannot be captured by the constant impedance model. On the other hand, the transient impedance model can help capture the unstable 20-Hz mode.

Remarks:

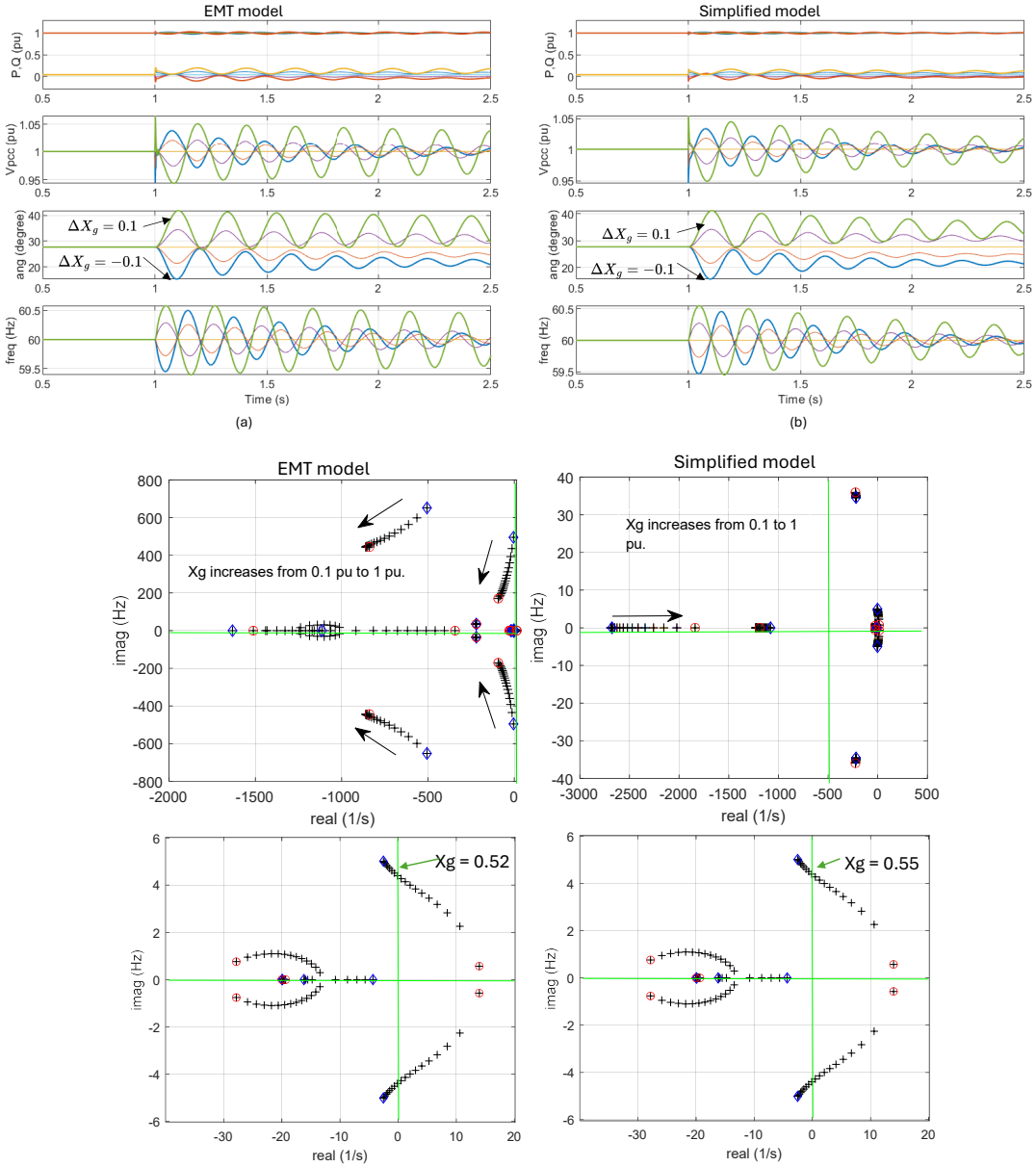

Fig. 11: The 4-Hz oscillation event. (a)(b) Comparison of simulation results of Model 1 (a, left column) and Model 2 (b, right column). At $t = 1$ s, the grid impedance changes. Four cases have been tested: $\Delta X_g = -0.1, -0.05, 0.05, 0.1$. (c) Eigenvalue loci for two modeling assumptions. Left column: Model 1-Detailed EMT model. Right column: Model 2. The plots in the lower row are the zoomed plots of those in the upper row.

- It can be seen for the 20-Hz oscillation event, Model 2 cannot be used to replace Model 1, since Model 2 is not able to create the 20-Hz oscillations. This shows that Model 2 has the critical dynamics not modeled. The critical dynamics is the real-part of the complex grid impedance, which cannot be adequately represented when a constant impedance is assumed.
- It can be seen for the 4-Hz oscillation event, Model 2 can be used to replace Model 1. In this case, the imaginary part of the complex grid impedance plays the dominant role of creating this dynamics. Using a constant impedance can adequately represent the imaginary part up to 20 Hz.

The discovery can be generalized. In the below 20-Hz region, if the real part of the complex grid impedance plays the major role, then the dynamics cannot be analyzed by use of constant grid impedance-based model. On the other hand, if the imaginary part of the complex grid impedance plays the major role, the dynamics can be analyzed by the constant grid impedance based model. Usually, in the below 10-Hz region, the magnitude of the real part is much less than that the imaginary part, implying the applicability of constant impedance-based models.

C. 8-Hz oscillation event

In the third case, an 8-Hz oscillation event is created. The PLL parameters are adjusted to be $(100, 2000)$, while the DC-link voltage control (instead of real power regulation) is adopted for the d-axis outer control. The DC-link voltage control's PI parameters are selected as $(1, 100)$. Furthermore,

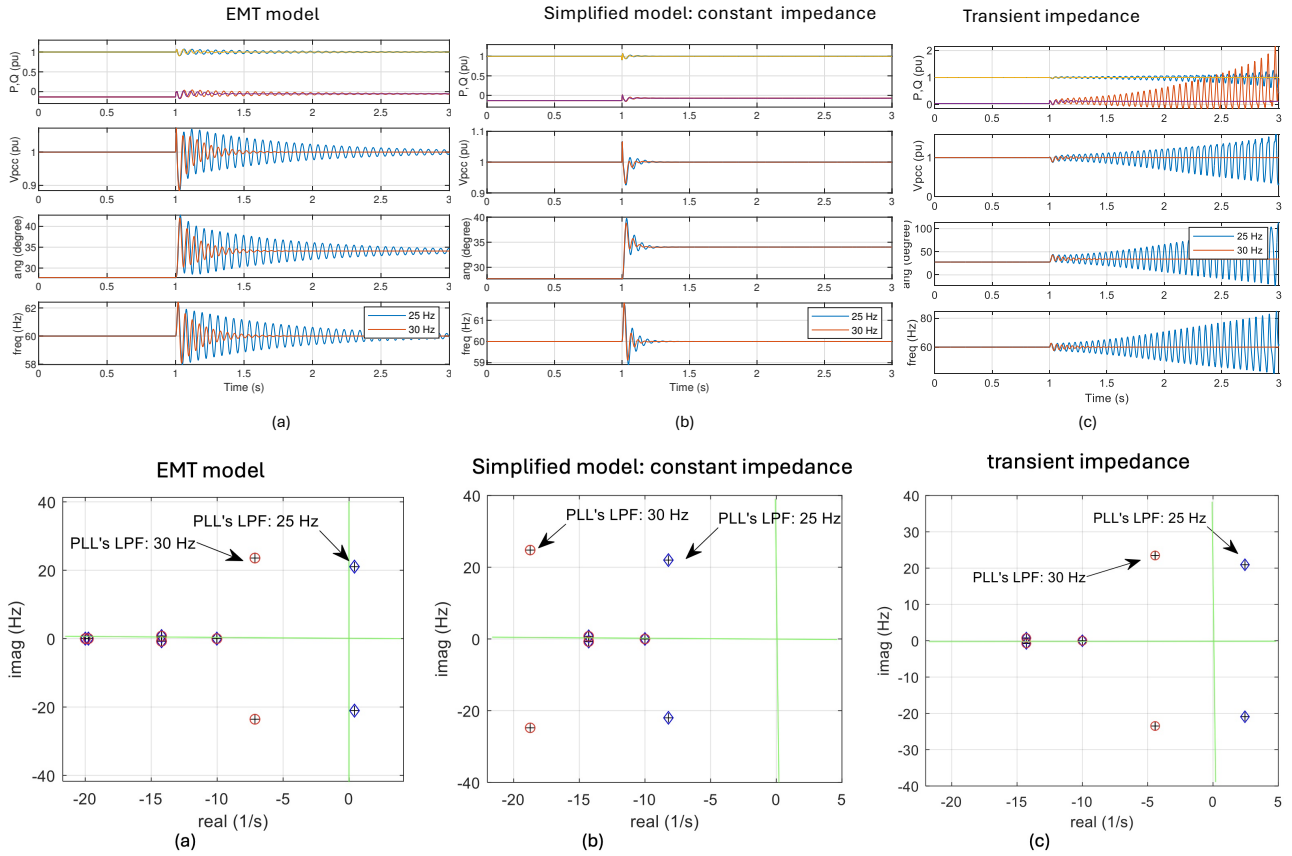

Fig. 12: The 20-Hz event. (a)-(c) Simulation results. (a) Model 1. (b) Model 2. (c) Model 3. At $t = 1$ s, the grid impedance changes. ; (d)-(f) Eigenvalue loci. (d) Detailed EMT model. (e) Model 2 based on constant impedance. (f) Model 3 based on transient impedance.

the AC voltage control's PI parameters are selected as $(1, 100)$. This set of parameters ensure that Block1 in Fig. 5(a) and G_{PLL} may interact and generate a resonance peak at 8 Hz. The DC-link's capacitor dynamics can be expressed in per unit power as follows:

$$\tau_{\text{DC}} \frac{dV_{\text{DC}}^2}{dt} = P_{\text{DC}} - P, \tag{28}$$

where τ is the time constant associated with the DC link capacitor size. A typical value of τ_{DC} is 0.026 s. This equation has been derived in [17].

The d-axis outer control has the DC-link voltage squared deviation ($V_{DC}^2 - 1$) as the input for a PI controller, and outputs the d-axis current order. If P_{DC} is treated as a constant, then i_d^* can be expressed as follows:

$$\Delta i_d^* = -\underbrace{\left[\frac{1}{\tau_{\text{DC}} s}\left(K_p + \frac{K_i}{s}\right)\right]}_{G_P} \Delta P \tag{29}$$

The time-domain simulation results using Model 1 and Model 2 are shown in Fig. 13(a), while the eigenvalue analysis results are shown in Fig. 13(b). It can be seen that the constant impedance representation of the grid can capture the 8-Hz oscillation. This pushes the application scope of the constant impedance assumption to model dynamics up to 10 Hz.

D. Series compensation

In the previous three cases, the transmission line is assumed to be an inductive circuit without any series compensation. In the final case, series compensation is included. Model 1, the EMT model, has been updated from the one used to generate 8-Hz oscillations to include line capacitor dynamics. There is no need to update Model 2. The objective of the case is to show that if the dominant dynamics have a bandwidth of less than 10 Hz, constant impedance-based models are sufficient to capture the dominant dynamics.

Fig. 14(a) shows the eigenvalues loci for a changing total grid impedance. The compensation level is maintained at 12%. The PLL's PI parameters have been tuned to be (200, 2000). The detailed EMT model has two modes in the subsynchronous region: a mode of 8 Hz, moving towards the right half-plane (RHP) when X_g increases; and a mode in the region of 50 Hz to 60 Hz, which moves towards the left half-plane (LHP) first and then to the RHP. The second mode is associated with series compensation.

The 8-Hz mode is the dominant mode when the grid strength is low or X_g is above 0.3 pu. Model 2, the constant impedance-based model, has only one oscillation mode at 8 Hz in the subsynchronous region. This comparison shows that Model 2 can capture the dominant dynamics.

Fig. 14(b) further shows simulation results. The system is subject to a line tripping event. The resulting grid strength reduces. For both models, they have the same initial condition

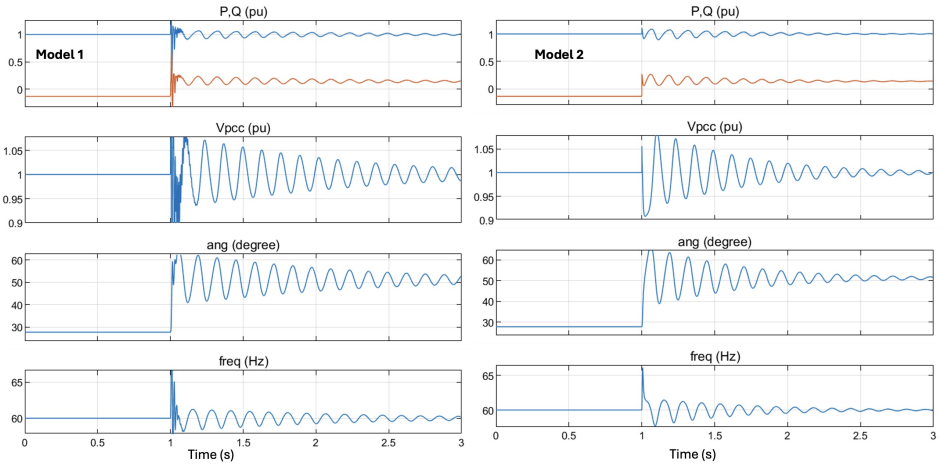

(a)

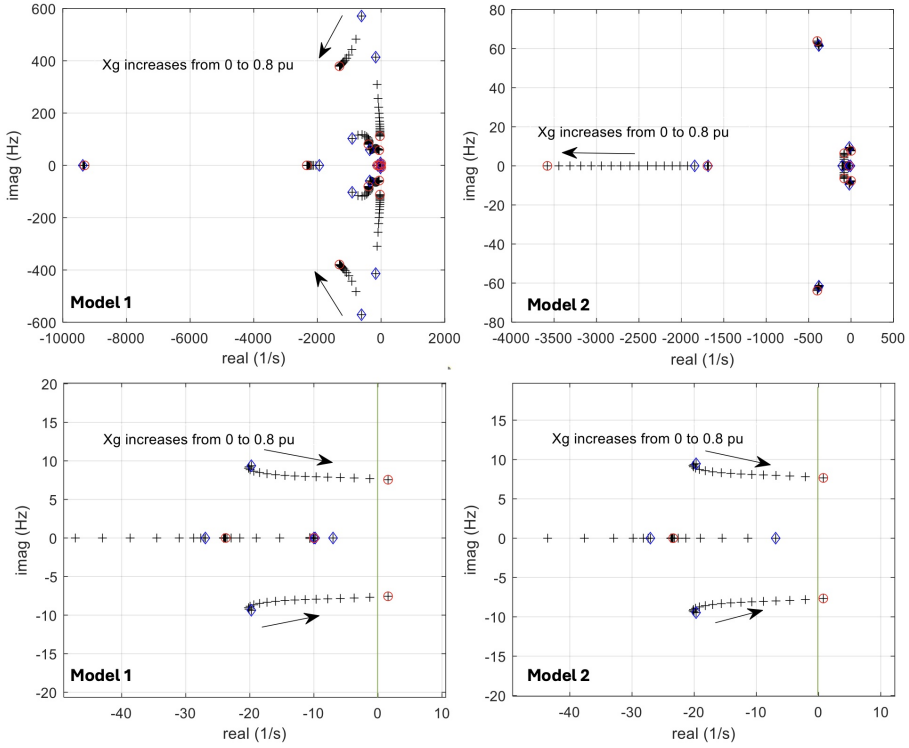

(b)

Fig. 13: The 8-Hz event. (a) Comparison of simulation results of Model 1 and Model 2. At $t = 1$ s, the grid impedance changes from 0.4 pu to 0.73 pu. (b) Eigenvalue loci. Left column: Detailed EMT model or Model 1. Right column: Model 2. The plots in the lower row are the zoomed plots of those in the upper row.

and the inductive line reactance is 0.5 pu while the series capacitor is 0.1 pu. For Model 1, line tripping leads to 0.37 pu grid impedance increase, while for Model 2, a line tripping event leads to 0.345 pu grid impedance increase. At these conditions, both models show sustained 8-Hz oscillations. While the simulation results do not exactly match each other, Model 2 is able to demonstrate 8-Hz oscillations when grid strength reduces. Furthermore, characteristics of the oscillations match well in both models. For example, oscillations in the voltage and angle measurements appear out of phase in both models; and oscillations in the real and reactive power measurements are in phase.

Fig. 14(c) compares transient stability using two models. The grid voltage is subject to a 42% voltage dip lasting 0.055 seconds. The PLL's output angle increases from 30 degrees to approximately 100 degrees in both cases. This voltage dip condition is a marginal condition for both models. A bit more voltage dip (e.g., 45%) leads to PLL loss of synchronism.

This numerical example confirms that the constant impedance based model (Model 2) is capable of capturing dynamics below 10 Hz region, even for a series compensated network. The eigenvalue results also show that Model 2 is not able to capture the LC dynamic mode. If this mode becomes dominant, when the compensation level is higher, Model 2 will not be able to capture the LC resonance related dynamics.

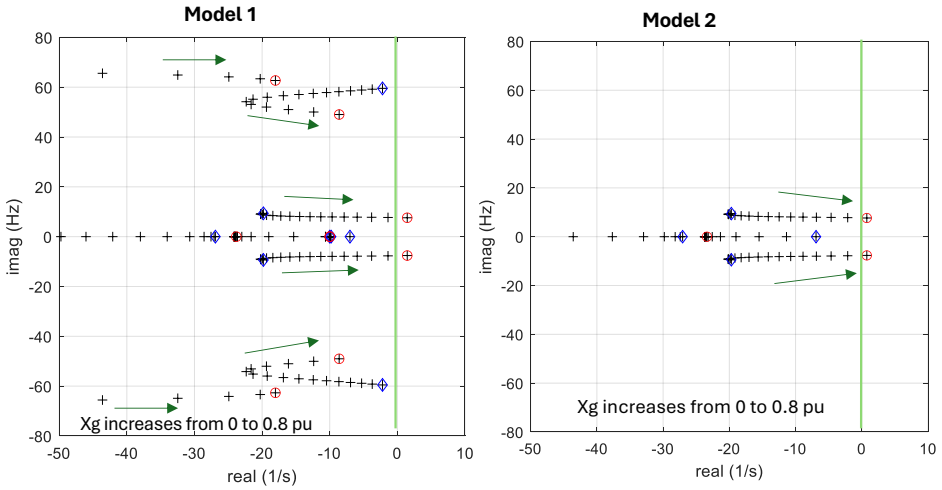

(a)

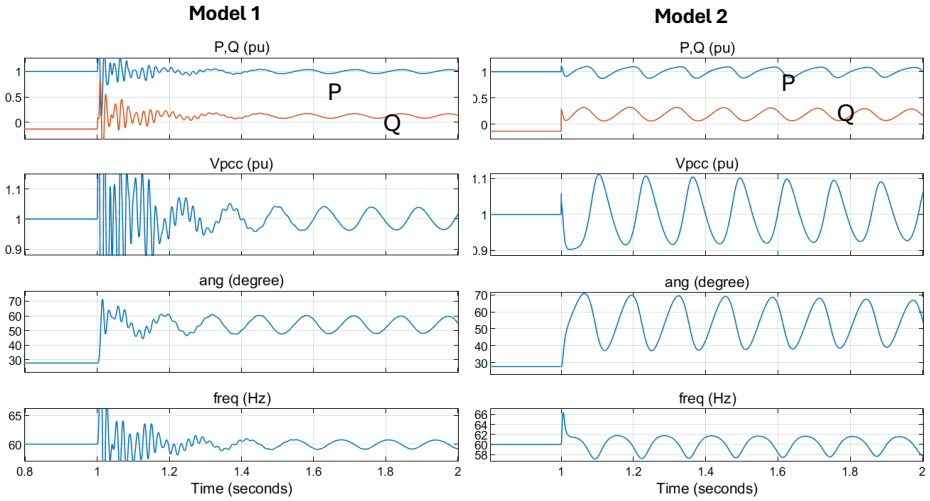

(b)

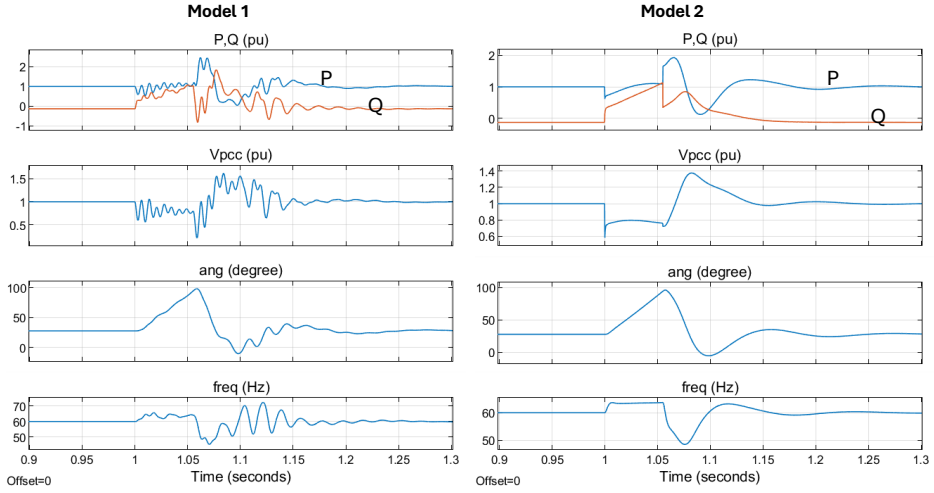

(c)

Fig. 14: Case 4: series compensated network. (a) Comparison of eigenvalues of Model 1 and Model 2. (b) Comparison of simulation results at the marginal conditions of sustainable 8-Hz oscillations. (c) Comparison of the system responses for low-voltage ride through, when the grid voltage is reduced to 0.58 pu at $t = 1$ s and lasted 0.055 s.

V. Conclusion

This research provides a theoretic analysis on why RMS-based dynamic simulation software packages can replicate some real-world events while they cannot in some other cases in grid-following IBR systems. Our paper shows the exact reason behind. The imaginary part of the grid impedance is almost constant for below 20-Hz region, while the real part's

magnitude is proportional to the frequency and its impact cannot be ignored for dynamics of above 10 Hz. Therefore, it can be seen that if the imaginary part of the impedance plays a dominant role (usually for dynamics of below 10-Hz), we can use the constant grid impedance assumption.

The findings are applicable to grid-following IBRs. For the grid-forming type power-based synchronization, the theoretic framework or the feedback system will be very different. How the real and imaginary parts of the complex grid impedance engage in the feedback system is also very different. Therefore, insights developed in this paper cannot be directly applied to a grid-forming IBR. Ref. [18] has shown a case where 6-Hz oscillations appear in a grid-forming IBR integration system due to series compensation. In the uncompensated case, there is no risk of oscillations in the approximate frequency region. This example implies that grid dynamics play a key role in creating 6-Hz oscillation. In this case, constant impedance model will not be able to capture the dynamics.

REFERENCES

[1] L. Fan, Z. Miao, and D. Ramasubramanian, "Transient algebraic impedance derivations and applications for pll-synchronized ibrs," *IEEE Transactions on Power Delivery*, vol. 39, no. 1, pp. 683–686, 2024.

[2] P. Sauer, B. Lesieutre, and M. Pai, "Transient algebraic circuits for power system dynamic modelling," *International Journal of Electrical Power & Energy Systems*, vol. 15, no. 5, pp. 315–321, 1993. [Online]. Available: https://www.sciencedirect.com/science/article/pii/014206159390053P

[3] S.-H. Huang, J. Schmall, J. Conto, J. Adams, Y. Zhang, and C. Carter, "Voltage control challenges on weak grids with high penetration of wind generation: Ercot experience," in *2012 IEEE Power and Energy Society General Meeting*. IEEE, 2012, pp. 1–7.

[4] C. Li and R. Reinmuller, "Asset condition anomaly detections by using power quality data analytics," in *2019 IEEE Power & Energy Society General Meeting (PESGM)*. IEEE, 2019, pp. 1–5.

[5] Julian Leslie. (2022, January) G-PST/ESIG Webinar Series: Managing Grid Stability in a High IBR Network. [Online]. Available: https://www.esig.energy/event/webinar-managing-grid-stability-in-a-high-ibr-network/

[6] Y. Cheng, L. Fan, J. Rose, S.-H. Huang, J. Schmall, X. Wang, X. Xie, J. Shair, J. R. Ramamurthy, N. Modi, C. Li, C. Wang, S. Shah, B. Pal, Z. Miao, A. Isaacs, J. Mahseredjian, and J. Zhou, "Real-world subsynchronous oscillation events in power grids with high penetrations of inverter-based resources," *IEEE Transactions on Power Systems*, vol. 38, no. 1, pp. 316–330, 2023.

[7] J. J. Sanchez-Gasca, S. D. Rao, and D. Ramasubramanian, "Modal analysis of a photovoltaic power plant in low short circuit grids modeled with generic models," in *2023 IEEE Power & Energy Society General Meeting (PESGM)*, 2023, pp. 1–5.

[8] J. Chow, J. Winkelman, M. Pai, and P. Sauer, "Singular perturbation analysis of large-scale power systems," *International Journal of Electrical Power & Energy Systems*, vol. 12, no. 2, pp. 117–126, 1990.

[9] O. Ajala, N. Baeckeland, B. Johnson, S. Dhople, and A. Domínguez-García, "Model reduction and dynamic aggregation of grid-forming inverter networks," *IEEE Transactions on Power Systems*, vol. 38, no. 6, pp. 5475–5490, 2023.

[10] L. Harnefors, "Modeling of three-phase dynamic systems using complex transfer functions and transfer matrices," *IEEE Transactions on Industrial Electronics*, vol. 54, no. 4, pp. 2239–2248, 2007.

[11] L. Fan, "Modeling type-4 wind in weak grids," *IEEE Transactions on Sustainable Energy*, vol. 10, no. 2, pp. 853–864, 2019.

[12] Y. Li, L. Fan, and Z. Miao, "Stability control for wind in weak grids," *IEEE Transactions on Sustainable Energy*, vol. 10, no. 4, pp. 2094–2103, 2019.

[13] R. Mittal, Z. Miao, and L. Fan, "Stability enhancement for ibrs operating in weak grids through proper coordination and control," *IEEE Transactions on Energy Conversion*, vol. 39, no. 3, pp. 1497–1508, 2024.

[14] L. Fan, Z. Miao, D. Piper, D. Ramasubramanian, L. Zhu, and P. Mitra, "Analysis of 0.1-Hz var oscillations in solar photovoltaic power plants," *IEEE Transactions on Sustainable Energy*, vol. 14, no. 1, pp. 734–737, 2022.

[15] L. Fan and Z. Miao, *Modeling and stability analysis of inverter-based resources*. CRC Press, 2023.

[16] D. Jovcic and L. Fan, "Analytical modeling of high-power converters: An approach for stability analysis of hvdc, facts, and wind power delivery systems," *IEEE Power and Energy Magazine*, vol. 23, no. 2, pp. 30–45, 2025.

[17] L. Fan and Z. Miao, "Wind in weak grids: 4 hz or 30 hz oscillations?" *IEEE Transactions on Power Systems*, vol. 33, no. 5, pp. 5803–5804, 2018.

[18] R. Mittal, Z. Miao, L. Fan, and D. Ramasubramanian, "Oscillation risks of grid-following and grid-forming inverter-based resources in series-compensated networks," *IEEE Transactions on Power Delivery*, 2025.

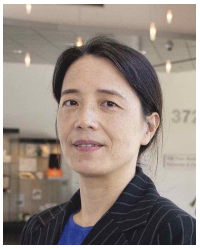

Lingling Fan (Fellow, IEEE) received the B.S. and M.S. degrees in electrical engineering from Southeast University, Nanjing, China, in 1994 and 1997, respectively, and the Ph.D. degree in electrical engineering from West Virginia University, Morgantown, in 2001. Currently, she is a professor at the University of South Florida inTampa Florida. Her research interests include power systems and power electronics. Dr. Fan served as Editor-in-Chief of *IEEE Electrification Magazine* from 2020 to 2024. She is the recipient of the 2024 Energy Systems Integration Group (ESIG) Excellent Award and the 2025 IEEE PES Wanda Reder Pioneer in Power Award.

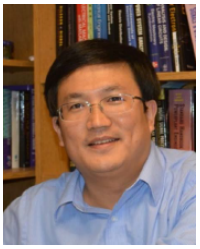

Zhixin Miao (Senior Member, IEEE) received the B.S. degree in electrical engineering from Huazhong University of Science and Technology, Wuhan, China, in 1992, the M.S. degree in electrical engineering from the Graduate School of Nanjing Automation Research Institute, Nanjing, China in 1997, and the Ph.D. degree in electrical engineering from West Virginia University, Morgantown, in 2002.

He is currently with the University of South Florida (USF), Tampa. Prior to joining USF in 2009, he worked in the Transmission Asset Management Department at Midwest ISO, St. Paul, MN, from 2002 to 2009. His research interests include power system stability, microgrids, and renewable energy. Dr. Miao aso serves as an Associate Editor for the *IEEE transactions on Sustainable Energy*.

Rahul Halugudde Ramakrishna (Graduate Student Member, IEEE) received the B.E degree from the Ramaiah Institute of Technology, Bangalore India in 2016, Master of Science degree, and Ph.D. degree from the University of South Florida (USF) in 2019 and 2025, respectively. He is currently with ETAP. His research interests include electromagnetic transient computer simulation for inverter-based resource generator interconnection.

Deepak Ramasubramanian (Senior Member, IEEE) received the M.Tech. degree from the Indian Institute of Technology Delhi, New Delhi, India, in 2013, and the Ph.D. degree from Arizona State University, Tempe, AZ, USA, in 2017. He is currently a Principal Technical Leader at the Grid Operations and Planning Group, Electric Power Research Institute (EPRI) and leads research projects related to modeling of inverter-based resources for bulk power system analysis.